



**Bimetallic Alloys in Action: Dynamic Atomistic Motifs for Electrochemistry and Catalysis**

Journal:	<i>Physical Chemistry Chemical Physics</i>
Manuscript ID:	CP-PER-04-2014-001591.R1
Article Type:	Perspective
Date Submitted by the Author:	11-Jun-2014
Complete List of Authors:	Mueller, Jonathan; University of Ulm, Institute of Electrochemistry Krtil, Petr; J. Heyrovsky Institute of Physical Chemistry, Kibler, Ludwig; University of Ulm, Institute of Electrochemistry Jacob, Timo; Universität Ulm, Institut für Elektrochemie

Cite this: DOI: 10.1039/c0xx00000x

www.rsc.org/xxxxxx

ARTICLE TYPE

# Bimetallic Alloys in Action: Dynamic Atomistic Motifs for Electrochemistry and Catalysis

Jonathan E. Mueller,<sup>a</sup> Petr Krtil,<sup>b</sup> Ludwig A. Kibler<sup>a</sup> and Timo Jacob<sup>a\*</sup>*Received (in XXX, XXX) Xth XXXXXXXXX 20XX, Accepted Xth XXXXXXXXX 20XX*

DOI: 10.1039/b000000x

Bimetallic alloys show great promise for applications in a wide range of technologies related to electrochemistry and heterogeneous catalysis. The alloyed nature of these materials supports the existence of surface phenomena and structural motifs not present in single-component materials. These novel features result in electrochemical and catalytic behaviors, requiring entirely new categories of explanations. In this perspective concrete examples are used to illustrate several of these chemical and structural features, which are unique to multi-component metal surfaces. The influence of the surface's structure and surroundings (e.g. adsorbates) on each other provides a common thread, with the emergence of dynamic surfaces as its terminus. In considering three model systems (PtRu, PtNi and AuPd), we discuss not only a selection of surface phenomena relevant to each, but also the implications of these alloy-related behaviors for the electrochemical and catalytic properties of each surface.

## 1. Introduction

Metal surfaces are indispensable in the overlapping fields of electrochemistry and heterogeneous catalysis. Both fields contain numerous examples of systems in which the atomic surface structure of a metal critically determines its behavior as an electrode or catalyst. Thus, the possible presence of surface defects is often an essential complication in satisfactorily accounting for a surface's electrochemical and catalytic properties. The introduction of a second metallic element to form a bimetallic system greatly increases the variety of surface structures possible, with important ramifications for the study and application of the surfaces of multi-component systems. One reason for this is that the greater variation in electrochemical and catalytic properties, corresponding to the larger number of possible structures, allows for greater optimization in the design of functional materials. However, an even more important reason is that structural motifs and surface phenomena, stemming from the chemical heterogeneity of the alloy, can lead to novel electrochemical and catalytic behaviors, with drastically improved performance for a given application.

In the context of heterogeneous catalysis and electrochemistry it is essential to distinguish between the reactivity of a surface and its catalytic activity. The reactivity of a surface directly reflects the strength of adsorption on it. Adsorption strength, however, depends not only on the nature of the surface, but also on the nature of the adsorbate. Nevertheless, if the varying reactivities of different adsorbates are factored out, then one arrives at a general reactivity for a surface, which is not just related to any one particular adsorbate, but characterizes the surface's contribution to the adsorption of any adsorbate. This surface reactivity is often expressed in terms of quantifiable electronic properties, such as

the *d*-band center.

Catalytic activity can only be specified in terms of a particular reaction, and characterizes the rate at which that reaction is catalyzed on the surface. Unlike its reactivity, a surface's catalytic activity cannot be naively abstracted away from particular catalytic reactions. Nevertheless, surface catalysis and reactivity are related, at least insofar as surface catalysis requires the adsorption of reactants (favored by high surface reactivity) and desorption of products (favored by low surface reactivity). By assuming that one of these two processes (i.e. reactant adsorption or product desorption) is rate-controlling, one is able to conclude that a surface with a reactivity that balances the rates of reactant adsorption and product desorption will display optimal (i.e. the highest attainable) catalytic activity. Indeed, similar lines of reasoning are commonly used to explain experimentally obtained volcano plots [1-7]. Thus, on one hand, it is essential to distinguish between the reactivity and catalytic activity of a metal surface. However, on the other hand, the relationship between the two can be taken advantage of in efforts to simply and efficiently predict catalytic behavior based on adsorption properties, albeit with caution.

In light of the chemical heterogeneity of bimetallic surfaces, at least three different classes of phenomena have been distinguished in efforts to explain their unique characteristics as electrodes and catalysts, i.e. their reactivity and catalytic activity [8]. These categories correspond to explanations which are derived from either i) bifunctional mechanisms, ii) delocalized electronic properties of the catalyst, or iii) the local atomic configuration of the catalyst surface.

In a bifunctional mechanism each component of the bimetallic alloy is responsible for either catalyzing a different reaction step

or adsorbing a different intermediate. This synergy between the two components results in increased catalytic activity. A classic example of bifunctional mechanisms at work is the electrooxidation of carbon monoxide, methanol and other small organics on PtRu alloys [9-15].

The delocalized electronic band structure of a bimetallic alloy varies from that of either pure metal and will have its own unique adsorption and catalytic properties. Thus, some aspect of the band structure of the surface as a whole is appealed to in order to explain the surface's reactivity towards adsorbates and catalytic activity. A prime example of this approach is the model developed by Hammer and Nørskov for adsorption on transition metal overlayer structures, from which they conclude that there is a direct relationship between the chemisorption energies of a given adsorbate on a transition metal heteroepitaxial monolayer on various transition metal substrates and the *d*-band center of the substrate metal [16-17]. This approach can be further extended to explain the catalytic activities of transition metal surfaces. Thus, plotting the experimental exchange currents as a function of the *d*-band center results in a so called volcano plot, whose apex corresponds to an optimal value for the *d*-band center, which can then be aimed at in the development of improved catalysts [18]. However, caution is required, as additional phenomena (e.g. surface reconstruction, restructuring, surface segregation) can result in surface properties significantly different than those predicted by a volcano plot.

Lastly, active sites corresponding to particular local atomic structures are sometimes implicated in the increased reactivity and catalytic activity often realized in bimetallic alloy catalysts.

Here, instead of delocalized perturbations in the electronic structure of the catalyst being responsible for increased catalytic activity, local arrangements of atoms (corresponding to local perturbations in the electronic structure) provide the key adsorption or critical catalytic active sites [8,19-20]. Metal surfaces have often been considered static under reaction or catalytic conditions; however, there is a growing body of evidence pointing toward dynamic surface structures for a number of metals under typical reaction conditions [21-22]. Such changes in a metal's surface structure naturally result in changes in its reactivity and catalytic activity, especially when particular local active sites are key players, since their presence or absence can result in drastic alterations in the overall chemical behavior of the surface. It is thus essential to take the actual structure of the surface under reaction or catalytic conditions into account, in explaining its behavior.

A number of excellent review articles already provide comprehensive overviews of the literature on bimetallic electrodes and catalyst surfaces, including their synthesis, characterization, atomic and electronic structures, physical, chemical and catalytic properties, and applications [23-27]. In contrast, the aim of this paper is to highlight those unique structural features of bimetallic surfaces, which set them apart from single metal surfaces, and then to consider the influence of these structural features on the electrochemical and catalytic properties of bimetallic surfaces. To facilitate this, three examples of bimetallic model electrodes/catalysts have been chosen as typical instances of phenomena pertinent to understanding the functionality of bimetallic surfaces under

electrochemical conditions: PtRu, NiPt and AuPd. Indeed, the study of model systems is an indispensable strategy in both heterogeneous catalysis and electrochemistry, because it enables one to consider relevant parameters in isolation, before attempting to put together a picture of the whole. In considering these three model systems, we begin by looking at the role played by average, delocalized electronic properties in PtRu alloys before turning to the role of local structures in NiPt and AuPd alloys. The influence of the catalytic environment on the catalyst's surface structure and composition, leading to a dynamic rather than static catalyst surface, is given special attention here, as a vital, but often overlooked, aspect of multi-component transition metal catalysts.

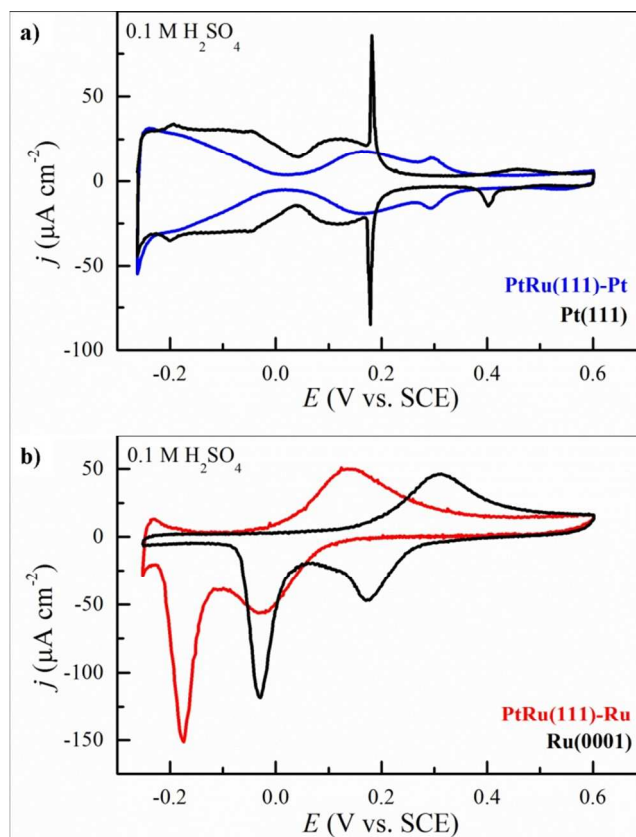


**Figure 1** Current-potential curves for: a) a Pt-enriched surface of PtRu(111) (blue curve), and Pt(111) (black curve), a) a Ru-enriched surface of PtRu(111) (red curve), and Ru(0001) (black curve). All scans were performed in 0.1 M H<sub>2</sub>SO<sub>4</sub> at a scan rate of 50 mVs<sup>-1</sup>. These measurements were carried out with the same electrode, and so one should note that the changes seen here as a function of sample preparation might also occur *in-situ* or *in-operando* for real systems. Adapted from Ref. [51].

## 2. ORR on PtRu: untangling strain and ligand effects

### 2.1 Introduction to PtRu alloys

The excellent catalytic properties of bimetallic PtRu alloys in the electro-oxidation of small organic molecules have long been recognized [10,13,28-29]. In particular, the low sensitivity of PtRu alloys to poisoning combined with the highly reduced overpotentials required for the oxidation of key intermediates

such as CO [30-35] have led to extensive studies of their structure and catalytic properties [36-44]. A number of different effects have been appealed to in explaining the catalytic activity of PtRu alloys in various reactions, including: i) bifunctional mechanisms, as in the case of oxidation reaction involving CO [10], ii) the ligand effect, resulting from the influence of neighboring atoms on the electronic states of surface atoms [34,45], iii) the strain effect resulting from altered nearest-neighbor distances in a pseudomorphically grown surface layer [46-47], and iv) the ensemble effect in which particular structural motifs of surface atoms serve as active sites [15,48].

## 2.2 Role of substrate vs. role of overlayer

The different reactivities of Ru and Pt can be taken advantage of to form segregated, pseudomorphic surface layers of either pure Pt or pure Ru on a PtRu low-index surface. Thus surface heating followed by cooling under an inert or reductive atmosphere results in the segregation of the less oxophilic Pt to the surface [49-51]. Similarly, surface heating followed by cooling under an oxidative (*i.e.* oxygen-containing) atmosphere draws Ru to the surface. Indeed, cyclic voltammetric measurements lead to the conclusion that the surface segregation in both cases is complete so that the surface layer is pure Pt in the former case and pure Ru in the latter [51]. In the case of the Pt-enriched surface, the base voltammogram in 0.1 M H<sub>2</sub>SO<sub>4</sub> (see **Figure 1a**) strongly resembles the characteristic base voltammogram for Pt(111) in the same electrolytic solution, with the cation (e.g. H<sup>+</sup>) adsorption peaks shifted to more negative and anion (e.g. HSO<sub>4</sub><sup>-</sup>) peaks shifted to more positive potentials, due to decreasing free energies of adsorption. In the case of the Ru-enriched surface, the base voltammogram in 0.1 M H<sub>2</sub>SO<sub>4</sub> (**Figure 1b**) shows the same characteristic peaks as the base voltammogram for Ru(0001) (the equivalent surface for an Ru, an hcp metal) in the same electrolytic solution, with the surface oxidation and reduction and hydrogen evolution peaks shifted by 200 mV to more negative potentials.

These two sets of voltammograms illustrate well the respective roles of the substrate and the surface in epitaxial catalysts. On one hand, the chemical nature of the surface determines the overall form of the cyclic voltammogram, *i.e.* the overall electrodynamic properties of the surface. On the other hand, the substrate alters the shape and potential placement of the peaks, *i.e.* influences the exact electrode potential at which individual reactions and adsorption events take place. In this particular example, the presence of more reactive Ru in the substrate decreases the reactivity of the Pt(111) surface (*i.e.* decreases the strength of adsorption to it), while the presence of less reactive Pt in the substrate increases the reactivity of a Ru(0001)/Ru(111) surface (*i.e.* increases the strength of adsorption to it). Thus placing an overlayer on a modified substrate is a useful strategy for modifying its catalytic properties in a controlled manner [52].

## 2.3 Disentangling the strain and ligand effects

### 2.3.1 Strategies for disentanglement

Of the effects which may contribute to the unique catalytic properties of bimetallic catalysts only the so called ligand and strain effects can be applied to epitaxial catalysts in which the surface is composed of atoms of only one component. In the first case the electronic influence of the substrate alters the adsorption

and catalytic properties of the surface, while in the second case the alteration in the chemical properties of the surface results from its taking on the lattice constant of the substrate. In practice these two effects are typically encountered simultaneously, and are thus difficult to distinguish. For example, a Pt(111) epitaxial layer on a PtRu alloy experiences both strain and ligand effects due to the PtRu substrate. Furthermore, any attempt to vary one of these effects by varying the composition of the alloy will cause a simultaneous (and likely proportional) effect in the other effect, since both effects are expected to be proportional to the fraction of Ru in the substrate. Nevertheless clever experimental or theoretical approaches are available for differentiating these effects.

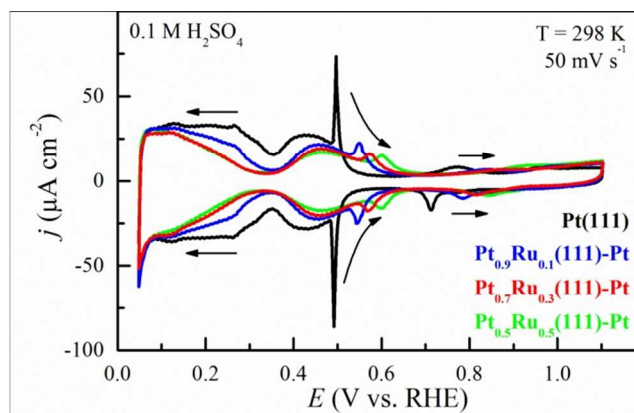


**Figure 2** Current-potential curves for Pt-rich surfaces of PtRu(111) electrodes of various alloy composition. All scans were performed in 0.1 M H<sub>2</sub>SO<sub>4</sub> at a scan rate of 50 mV s<sup>-1</sup>. [55]

One of the first approaches to disentangling the strain and ligand effects made use of the varying length scales over which they are expected to exert influence [53]. The ligand effect is expected to die out very quickly once the epitaxial layer is more than a monolayer thick. In contrast, in this particular case the strain on epitaxial layers due to lattice mismatch does not relax until the epitaxial layer is several monolayers thick. Thus, while an epitaxial monolayer exhibits both effects, an epitaxial layer composed of several monolayers exhibits primarily the strain effect. Based on this assumption Schlapka *et al.* have employed a combination of experiment and theory to disentangle strain and the ligand effect in the adsorption of CO on Pt(111) epitaxial layers on Ru(0001) under ultra high vacuum (UHV) conditions. The application to electrochemical systems was made shortly thereafter by Zhang *et al.*, who considered the ORR on Pt overlayers on transition metal substrates with varying strains and ligand effects [47]. More detailed insight was obtained by Hoster *et al.* [54] by considering the electrochemical adsorption of OH<sub>ad</sub> and H<sub>ad</sub> on Pt(111) overlayers of varying thicknesses on a Ru(0001) substrate. To probe the influence of various degrees of coupled strain and ligand effects on the electrochemical properties of a Pt(111) monolayer, cyclic voltammetric measurements have been carried out on Pt heteroepitaxial overlayers on PtRu substrates of various compositions. As can be seen in **Figure 2**, the extent of the deviation of the CV from that of pure Pt is directly related to the composition of the substrate, with more Ru resulting in greater deviation. Because there is an approximately linear relationship between the composition and

the lattice parameter of the substrate, both the ligand effect and the strain effect are present in this system in similar proportions, making it very difficult, if not impossible, to disentangle them experimentally.

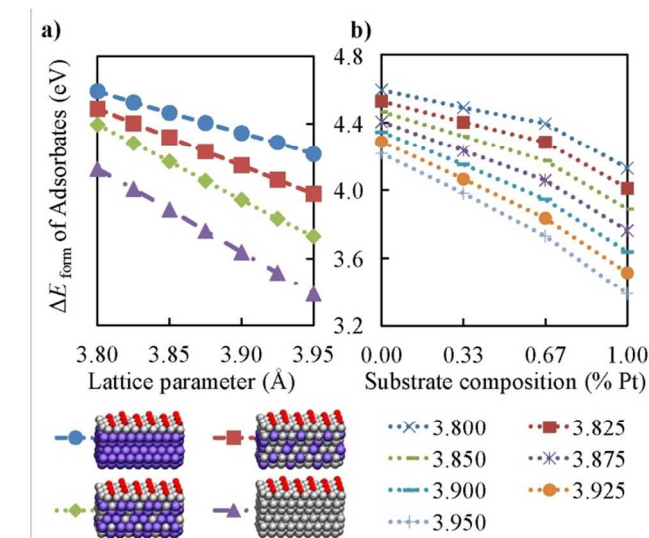


**Figure 3** Energies of formation (eV) per  $p(2 \times v3)$  unit cell for  $1/3$  ML of oxygen on a Pt(111) overlayer on PtRu substrate slabs with various PtRu compositions (corresponding to the ligand effect; these are reported as % Pt, and correspond to compositions for the 5 substrate layers—i.e. excluding the  $Pt_6$  overlayer—of  $Ru_{30}$ ,  $Pt_{10}Ru_{20}$ ,  $Pt_{20}Ru_{10}$  &  $Pt_{30}$ ) and unit cell parameters (corresponding to the strain effect; these are reported as the corresponding fcc cubic unit cell dimension in Angstroms). Reference states are  $H_2$  gas,  $H_2O$  gas and the corresponding bare PtRu-Pt(111) slab. The same 28 energies are plotted twice: **a**) as a function of the unit cell parameter and **b**) as a function of substrate composition. Red atoms are O, purple atoms are Ru and silver atoms are Pt.

### 2.3.2 Surface adsorption

To gain more detailed insight into the respective roles of the strain and ligand effects on the catalytic characteristics of Pt(111) epitaxial layers on PtRu alloys, we performed a systematic DFT study of the adsorption energies of key intermediates and the reaction energies of critical steps in the oxygen reduction reaction (ORR) on Pt(111) as functions of the lattice constant (i.e. the strain effect) and the substrate composition (i.e. the ligand effect), which were varied independently. Along similar lines, related approaches have already been applied to Pd(111) overlayers on transition metal substrates [56-57].

**Figure 3** shows the adsorption energies for  $O_{ad}$  on a Pt(111) epitaxial layer on PtRu substrates of various compositions plotted as a function of the unit cell parameter in **Figure 3a**), then again as a function of the substrate composition in **Figure 3b**). The dependence of the adsorption energy on the unit cell parameter is strongly linear for the range of values checked ( $3.80 \text{ \AA} - 3.95 \text{ \AA}$ ), which correspond to the region between and immediately outside of the equilibrium unit cell parameters for pure Ru ( $\sim 3.825 \text{ \AA}$ ) and pure Pt ( $\sim 3.925 \text{ \AA}$ ) substrates. The slope shows a pronounced dependence on the composition of the substrate, as it nearly doubles from  $2.51 \text{ eV/\AA}$  to  $4.93 \text{ eV/\AA}$  as a pure Ru substrate is replaced with pure Pt. The dependence on the substrate composition is not linear, but is more pronounced for higher fractions of Pt, regardless of unit cell parameter. Because of this, the fractions change in adsorption energy attributable to the strain

and ligand effects for a change in substrate will vary depending on which path is taken between them. Thus exchanging a pure Pt substrate at equilibrium (unit cell parameter =  $3.925 \text{ \AA}$ ) for a pure Ru substrate at equilibrium (unit cell parameter =  $3.825 \text{ \AA}$ ) results in O adsorption which is  $1.02 \text{ eV}$  weaker,  $0.50 \text{ eV}$  of which would be attributed to the ligand effect if the substrate were to be compressed before replacing the Pt with Ru, which would then result in another  $0.52 \text{ eV}$  weakening in the adsorption. However if the Pt is replaced with Ru before compression, then the ligand affect accounts for  $0.77 \text{ eV}$  of the  $1.02 \text{ eV}$  total adsorption energy change, and the strain effect for only  $0.24 \text{ eV}$ .

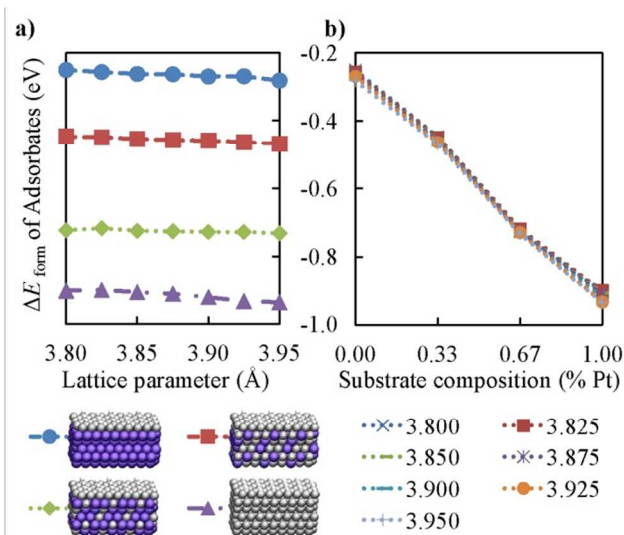


**Figure 4** Energies of formation (eV) per  $p(2 \times v3)$  unit cell for  $1/3$  ML of hydrogen on a Pt(111) overlayer on PtRu substrate slabs with various PtRu compositions (corresponding to the ligand effect; these are reported as % Pt, and correspond to compositions for the 5 substrate layers—i.e. excluding the  $Pt_6$  overlayer—of  $Ru_{30}$ ,  $Pt_{10}Ru_{20}$ ,  $Pt_{20}Ru_{10}$  &  $Pt_{30}$ ) and unit cell parameters (corresponding to the strain effect; these are reported as the corresponding fcc cubic unit cell dimension in Angstroms). Reference states are  $H_2$  gas and the corresponding bare PtRu-Pt(111) slab. The same 28 energies are plotted twice: **a**) as a function of the unit cell parameter and **b**) as a function of substrate composition. White atoms are H, purple atoms are Ru and silver atoms are Pt.

**Figure 4a** shows the adsorption energies for  $H_{ad}$  on a Pt(111) epitaxial layer on PtRu substrates of various compositions plotted as a function of the unit cell parameter, while **Figure 4b** shows the same set of adsorption energies plotted as a function of the substrate composition. The dependence of the adsorption energy on the unit cell parameter is strongly linear for the range of values checked ( $3.80 \text{ \AA} - 3.95 \text{ \AA}$ ), as is the dependence on the substrate composition for the compositions checked. In contrast to the case of O adsorption, H adsorption shows very little dependence on the unit cell parameter. Thus almost the entire  $0.67 \text{ eV}$  weakening of H adsorption upon replacement of a pure Pt substrate at equilibrium with a pure Ru substrate at equilibrium can be attributed to the ligand effect.

Analogous results for  $OH_{ad}$  reveal a case in which the two effects are equal: compression (from  $3.925$  to  $3.825 \text{ \AA}$ ) and substrate replacement (from pure Pt to pure Ru) each decrease the binding energy by  $0.11 \text{ eV}$ , regardless of the order in which they are carried out, for a net decrease of  $0.22 \text{ eV}$ . Thus, we see the

relative contributions of the strain and ligands effect ranging from contributing equally in the case of OH adsorption, to the ligand effect dominating the changes observed in the case of H adsorption, with the case of O adsorption lying in between. However, in all cases considered, both the strain and ligand effects resulting from replacing a Pt substrate with Ru substrate work together in weakening adsorption.

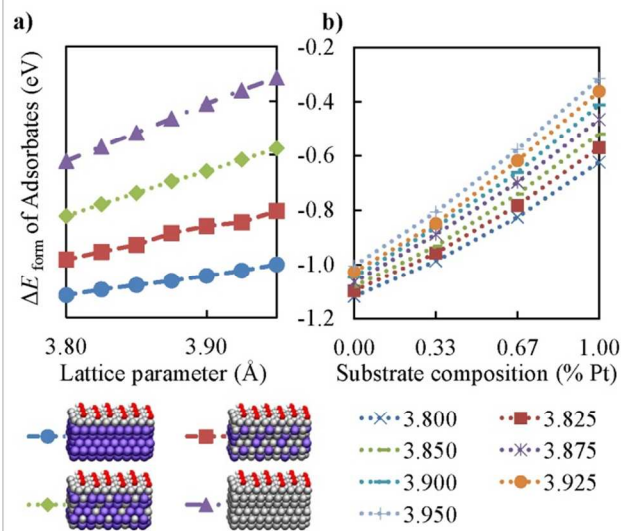


**Figure 5** Reaction energies (eV) per  $p(2 \times v_3)$  unit cell for the formation of  $1/3$  ML of OH from  $1/3$  ML each of preadsorbed O and H on a Pt(111) overlayer on PtRu substrate slabs with various PtRu compositions (corresponding to the ligand effect; these are reported as % Pt, and correspond to compositions for the 5 substrate layers—i.e. excluding the  $Pt_6$  overlayer—of  $Ru_{30}$ ,  $Pt_{10}Ru_{20}$ ,  $Pt_{20}Ru_{10}$  &  $Pt_{30}$ ) and unit cell parameters (corresponding to the strain effect; these are reported as the corresponding fcc cubic unit cell dimension in Angstroms). The same 28 resulting reaction energies are plotted twice: **a)** as a function of the unit cell parameter and **b)** as a function of substrate composition. Red atoms are O, white atoms are H, purple atoms are Ru and silver atoms are Pt.

### 2.3.3 Surface catalysis

Having considered the influence of the strain and ligand effects on several adsorbates we now turn our attention to model surface reactions, where we consider first the formation of  $OH_{ad}$  from  $O_{ad}$  and  $H_{ad}$ , followed by the dissociation of  $O_{2,ad}$  to form  $O_{ad}$ . The reaction energies for the first of these reactions, the formation of  $OH_{ad}$ , on Pt(111) overlayers on our 28 test substrates are presented in **Figure 5**. The dependence of the reaction energy on the strain is approximately linear for fixed substrate compositions. Similarly, the dependence of the reaction energy on the substrate composition is approximately linear for fixed values of the lattice parameter. The overall result of replacing Pt (at equilibrium) with Ru (at equilibrium) is a decrease in the exothermic reaction energy by 0.74 eV, making the reaction energy more negative, i.e. more exothermic. If the overlayer is compressed before the composition of the substrate is changed, the strain effect contributes  $-0.21$  eV; however, if the slab is compressed after the Pt substrate has been replaced with Ru, then the compression only results in a change of  $-0.07$  eV. The replacement of Pt with Ru in the substrate results in changes of  $-0.53$  and  $-0.67$  eV to the reaction energy respectively.

In the case of  $O_{2,ad}$  dissociation (**Figure 6**), replacing a pure Pt substrate at equilibrium with a pure Ru substrate at equilibrium

decreases the exothermicity of the reaction by 0.67 eV, from  $-1.22$  eV to  $-0.55$  eV. If the substrate composition is changed before the slab is compressed, then the ligand effect accounts for a strong majority (0.52 eV out of 0.67 eV) of this change, however if the order is reversed then compression and substitution yield equal contributions of 0.34 eV. Thus, the strain effect plays a more prominent role in the case of  $O_{2,ad}$  dissociation than in the case of  $OH_{ad}$  formation. However, we should note that for the first time we observe dependence on the subsurface composition which is non-linear. This step-like dependence in **Figure 6b)** reflects a similar non-linear dependence of the  $O_{2,ad}$  adsorption energy on composition, which has not yet been satisfactorily explained.

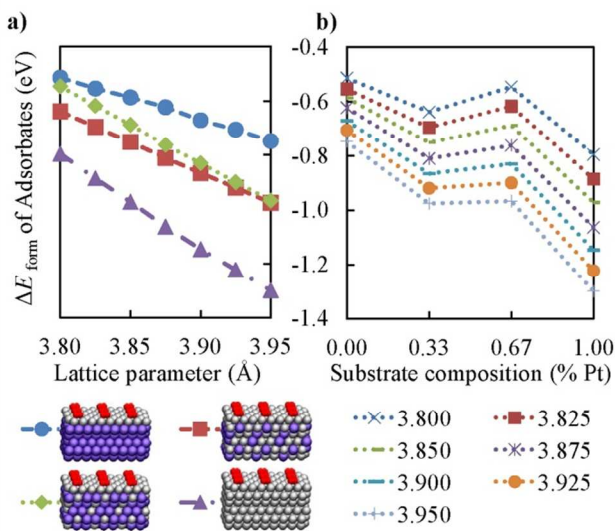


**Figure 6** Reaction energies (eV) per  $p(2 \times v_3)$  unit cell for the dissociation of  $1/6$  ML of  $O_2$  to form  $1/3$  ML each of adsorbed O on a Pt(111) overlayer on PtRu substrate slabs with various PtRu compositions (corresponding to the ligand effect; these are reported as % Pt, and correspond to compositions for the 5 substrate layers—i.e. excluding the  $Pt_6$  overlayer—of  $Ru_{30}$ ,  $Pt_{10}Ru_{20}$ ,  $Pt_{20}Ru_{10}$  &  $Pt_{30}$ ) and unit cell parameters (corresponding to the strain effect; these are reported as the corresponding fcc cubic unit cell dimension in Angstroms). The same 28 resulting reaction energies are plotted twice: **a)** as a function of the unit cell parameter and **b)** as a function of substrate composition. Red atoms are O, purple atoms are Ru and silver atoms are Pt.

Teasing out the concrete implications of the strain and ligand effects for a process, such as the oxygen reduction reaction (ORR), requires making assumptions regarding the rate limiting process and how it is affected by the strain and ligand effects respectively. We have already seen that the reaction energies for  $O_{2,ad}$  dissociation and  $OH_{ad}$  formation show opposite trends in response to both the strain and ligand effects. Thus, one might suppose (as is often done) that a compromise between these two (or two other analogous) reactions is required, and that the best attainable catalyst will support each reaction equally. A more rigorous approach would be to calculate the barriers for the individual steps in the ORR, as has already been done for Pt(111) [58–59], as a function of substrate composition/lattice constant. These barriers could then be used in a kinetic model for the ORR. The optimal catalyst would then be the catalyst with the fastest overall rate in the kinetic model. In fact, the laterally compressed Pt(111) surfaces of  $Pt_{0.7}Ru_{0.3}(111)$  and  $Pt_{0.9}Ru_{0.1}(111)$  exhibit

enhanced ORR activities compared with pure Pt(111) when studied in 0.1 M HClO<sub>4</sub> and 0.1 M H<sub>2</sub>SO<sub>4</sub>, respectively. An enhancement in ORR activity has also been observed for PtRu surface alloys on a Ru(0001) substrate [60].

### 3. Hydrogen adsorption on Pt<sub>3</sub>Ni alloys: surface site selectivity and reversible surface segregation

#### 3.1 Introduction to PtNi alloys

As one of the most promising catalysts for the ORR in acidic media, PtNi alloys have received a great deal of attention over the past decade in the search for efficient oxygen reduction catalysts for cathode materials in polymer electrolyte membrane fuel cells (PEMFC), [61-70]. The outstanding performance of Pt<sub>3</sub>Ni catalysts has been attributed by some groups to a *d*-band shift [18,71], while others have argued that it is due to a decrease in the lattice parameter that results from the alloying [72] (in analogy to the strain effect), and still others have sought to understand the catalytic behavior in terms of local atomic configurations at the surface [70,73-74]. Consideration of the combination of a stable noble metal (Pt) with a reactive transition metal (Ni), which is unstable at operating conditions (i.e. at positive potentials in acid media), stresses the importance of the catalysts stability and also of the dynamics of the alloy catalyst during operation. Another important consideration for Pt<sub>3</sub>Ni catalysts is the selective surface segregation observed in experiments [75-79], whose influence on their catalytic properties has been considered theoretically [80]. Here, we use Pt<sub>3</sub>Ni to consider, first, the role of local surface configurations followed by the influence of adsorbates on surface segregation.

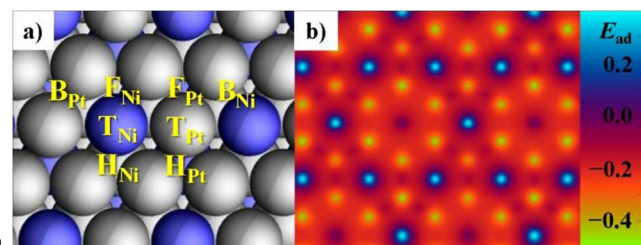


**Figure 7** a) Diagram of high-symmetry adsorption sites on Pt<sub>3</sub>Ni(111). T = top  $\equiv \mu_1$ , B = bridge  $\equiv \mu_2$ , F = fcc  $\equiv \mu_3$ , H = hcp  $\equiv \mu_3$ ; “pt” denotes a site adjacent to only Pt atoms; “ni” denotes a site with a neighboring Ni atom. Blue atoms are Ni and silver atoms are Pt. b) Potential energy surface for hydrogen adsorption on Pt<sub>3</sub>Ni(111). Adsorption energies ( $E_{ad}$  in eV) are referenced to gas phase H<sub>2</sub>.

**Table 1** Adsorption energies (eV) for hydrogen at high symmetry sites on Pt(111) and Pt<sub>3</sub>Ni(111) referenced to gas phase H<sub>2</sub>.

Substrate	Adsorption site	Adsorption energy (eV)
Pt(111)	fcc	-0.41
	hcp	-0.38
	top	-0.49
Pt <sub>3</sub> Ni(111)	fcc-Ni	-0.46
	fcc-Pt	-0.40
	hcp-Ni	-0.43
	hcp-Pt	-0.36
	top-Ni	-0.01
	top-Pt	+0.38

#### 3.2 Site selectivity for hydrogen adsorption

To illustrate site selectivity in bimetallic catalysts, we first consider the case of hydrogen adsorption on a Pt<sub>3</sub>Ni(111) surface, in the absence of surface segregation. The case of oxygen adsorption (along with hydrogen adsorption) has been considered by Jacob *et al.* [73-74], while the influence of only subsurface Ni on ORR reaction energies and barriers has been computed by Sha *et al.* [70].

If we consider a Pt<sub>3</sub>Ni(111) surface, in which the Ni atoms are evenly spaced and isolated, then each type of high symmetry site (T = top  $\equiv \mu_1$ , B = bridge  $\equiv \mu_2$ , F = fcc  $\equiv \mu_3$ , H = hcp  $\equiv \mu_3$ ) can be further divided into sites with an adjacent Ni atom (T<sub>Ni</sub>, B<sub>Ni</sub>, F<sub>Ni</sub> & H<sub>Ni</sub>) and sites having only Pt nearest neighbors (T<sub>Pt</sub>, B<sub>Pt</sub>, F<sub>Pt</sub> & H<sub>Pt</sub>), as illustrated in **Figure 7**. In **Table 1**, we compare hydrogen adsorption energies to these two different categories of sites on Pt<sub>3</sub>Ni(111) along with Pt(111). The presence of Ni increases site selectivity of hydrogen adsorption on the surface. In particular, hydrogen now selectively adsorbs at sites where it comes into direct contact with a Ni surface atom. As a result the potential energy landscape of the surface with respect to hydrogen adsorption becomes substantially rougher, with adsorption-potential-energy wells centered on surface Ni atoms. Thus, instead of being relatively free to move across the surface—as on Pt(111) where adsorption energies to the various binding sites fall within a  $\sim 0.1$  eV range—adsorbed hydrogen will tend to get trapped within the immediate vicinity of Ni surface atoms.

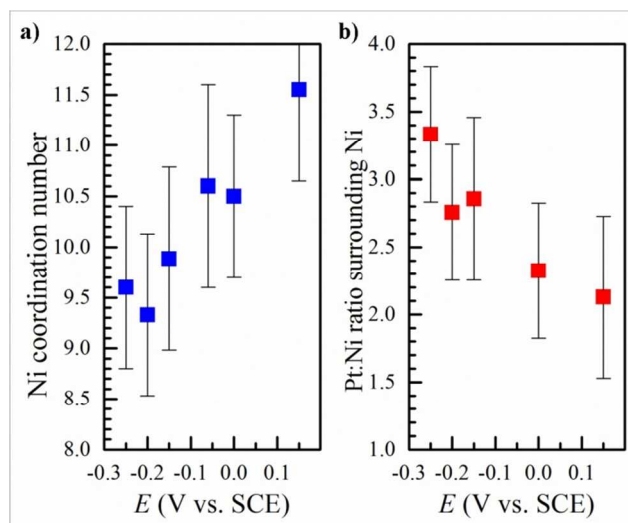


**Figure 8** a) Average coordination number (CN) and b) local chemical composition in the vicinity of Ni for a nafion-stabilized nanoparticulate Pt<sub>3</sub>Ni electrode, polarized at various potentials in the H<sub>UPD</sub> region. Local chemical composition was calculated from independently refined Pt and Ni occupancy in the first coordination shell. Adapted from Ref. [81].

#### 3.3 Adsorbate-induced surface segregation

Motivated by this theoretically predicted restricted mobility of the adsorbed hydrogen, the local structure of the nanoparticulate Pt<sub>3</sub>Ni (*d* = 5 nm) carbon supported catalyst in 0.1 HClO<sub>4</sub> was assessed using X-ray adsorption spectroscopy. Here, the Ni *K* edge and Pt *L3* edge X-ray absorption spectra (XAS) were recorded under conditions corresponding to hydrogen underpotential deposition (H<sub>UPD</sub>). When subject to a full profile refinement, the extracted extended X-ray absorption fine structure

(EXAFS) function yields average coordination numbers for each alloy's constituent. These coordination numbers reflect the distribution of each constituent between catalyst surface and bulk

sites, along with the local chemical composition and bond distances of neighboring atoms.

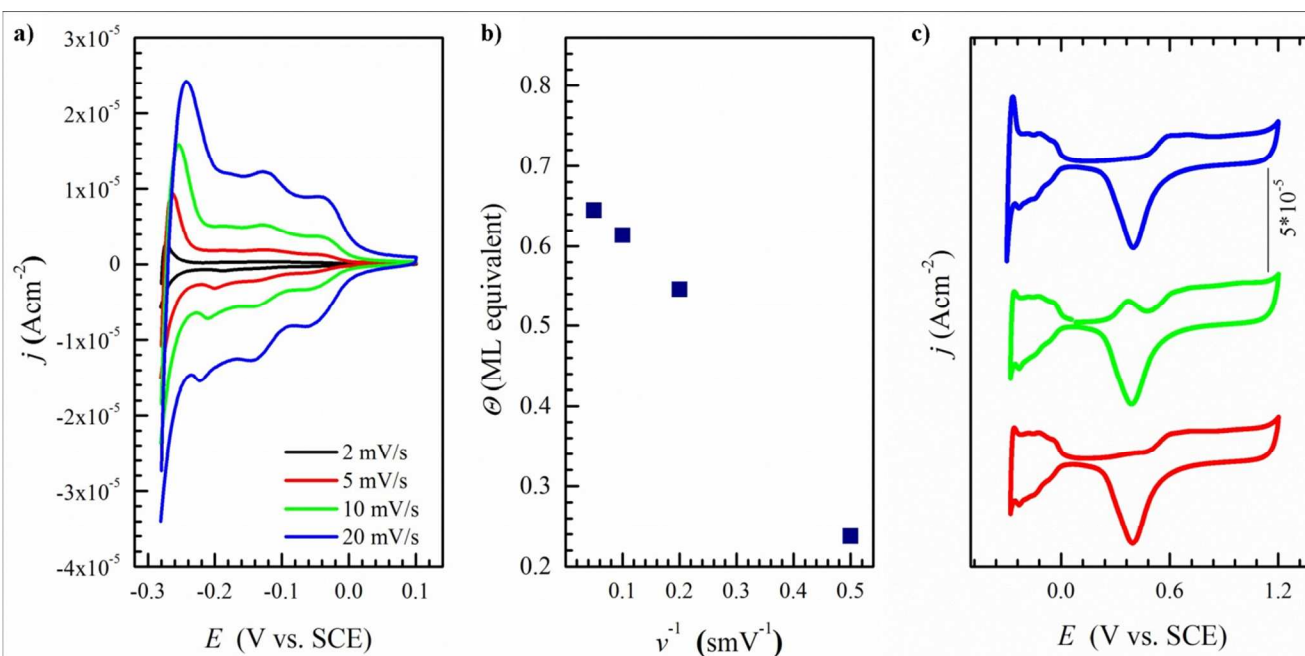


**Figure 9** a) Voltammetric curves and b) integrated charge of the underpotential deposition of hydrogen on a Pt<sub>3</sub>Ni nanoparticulate electrode in 0.05 M H<sub>2</sub>SO<sub>4</sub> recorded consecutively at various polarization rates (see figure legend). c) Comparison of the last voltammogram recorded before polarization in the H<sub>UPD</sub> region (blue curve) with the first two cycles (green and red curves respectively) recorded after cycling the electrode in the H<sub>UPD</sub> region for 2 hours. All voltammograms in c) were recorded at the polarization rate of 20 mV/s. Adapted from Ref. [81].

The results of the *in-situ* XAS paint a dynamic picture of the Pt<sub>3</sub>Ni catalyst's structure. The combination of the coordination number (CN) and local chemical composition (expressed as a Pt/Ni ratio) indicates that Ni is primarily confined to sub-surface sites at potentials outside the hydrogen adsorption region. The decrease in the Ni coordination number from 11.5 to 9.5 (see **Figure 8**) following the polarization of the Pt<sub>3</sub>Ni catalyst to the hydrogen adsorption region suggests a gradual transfer of Ni from the bulk to surface sites, as a result of hydrogen adsorption. The chemical composition of the Ni environment shows a complementary effect when the local Ni content relaxes from slightly over-stoichiometric value in the double layer region (when the Ni is confined to the bulk) to that approaching the average chemical composition once the presence of the Ni in the surface becomes possible.

The transfer and subsequent accumulation of Ni in the surface also manifests itself in the voltammetric behavior of the Pt<sub>3</sub>Ni catalysts cyclically polarized in the H<sub>UPD</sub> region. The charge corresponding to the hydrogen adsorption gradually decreases with decreasing polarization rate as well as with the total time the catalysts resides in the H<sub>UPD</sub> potential region (see **Figure 9**). A direct link between hydrogen adsorption and Ni accumulation in the surface confirming the *in-situ* XAS experiments gives the clear stripping signal of the accumulated Ni if the Pt<sub>3</sub>Ni catalyst is polarized to sufficiently positive potentials following the extensive polarization of the Pt<sub>3</sub>Ni catalysts in the H<sub>UPD</sub> region. The observed behavior also stresses the essential instability of the Pt<sub>3</sub>Ni catalysts at potentials characteristic of the ORR process, hence kinetic stabilization of Pt<sub>3</sub>Ni catalysts is prerequisite for the

application of these catalysts in the cathode reaction of fuel cells.

To confirm the responsibility of adsorbate hydrogen for reversing the surface segregation of the Pt<sub>3</sub>Ni nanoparticles, DFT calculations were performed examining the effect of hydrogen adsorbates on surface segregation for a Pt<sub>3</sub>Ni(111) slab. These surface segregation energies are presented in **Figure 10**, where the influence of 1/4 ML of atomic oxygen is also shown for the sake of comparison. As can be seen in the figure, the presence of adsorbed hydrogen stabilizes Ni atoms in the surface due to the strength of Ni–H bonds in comparison to Pt–H bonds, as was shown in the previous section. Thus, the DFT calculations confirm that adsorbed hydrogen is capable of inducing a change in the surface composition of the Pt<sub>3</sub>Ni nanoparticles by stabilizing Ni atoms in the particle surface. The experiments show that this change in surface composition takes place on the order of seconds and is reversible as depicted in **Figure 11**. Thus, Pt<sub>3</sub>Ni alloys provide us not only with an example of adsorbate-induced surface segregation, but reversible surface segregation, in which the catalyst's structure (and thus catalytic nature) is altered only temporarily during catalysis due to the adsorption of intermediates.

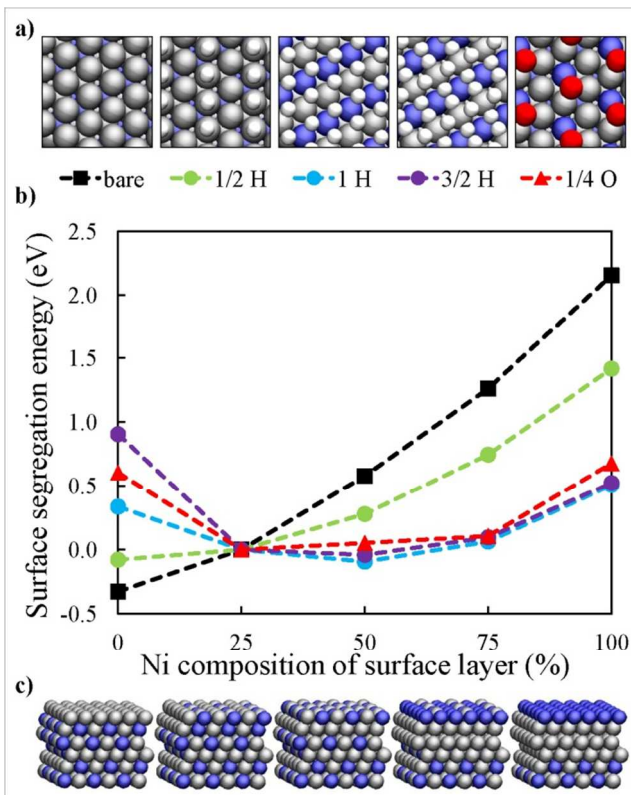


**Figure 10** a) Top views of slabs illustrating the most stable adsorbate configuration and metal surface composition at each coverage considered. The coverages correspond to the legend in **b)** directly below them. **b)** Surface segregation energies (eV) per  $2 \times 2$  unit cell for  $\text{Pt}_3\text{Ni}$  slabs with no adsorbates,  $\frac{1}{2}$  ML H, 1 ML H,  $1\frac{1}{2}$  ML H, and  $\frac{1}{4}$  ML O. Surface compositions are (left to right) 0%, 25%, 50%, 75% and 100% Ni. H atoms are white, Ni atoms are blue, O atoms are red, and Pt atoms are gray. **c)** Side views of slabs along the bottom illustrate Ni-Pt layer composition for various surface segregation states and correspond to the compositions along the x-axis in **b)** directly above them. Red atoms are O, white atoms are H, blue atoms are Ni and silver atoms are Pt. Adapted from Ref. [81].

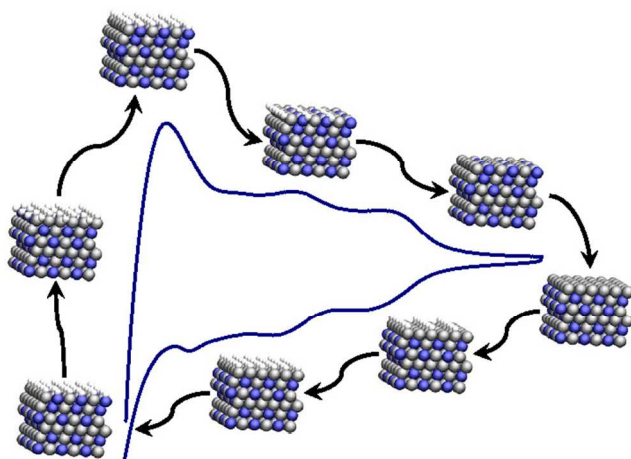


**Figure 11** Schematic of adsorbate-induced surface segregation, in which the presence of adsorbed hydrogen induces a change in the surface composition within an experimentally relevant timeframe. White atoms are H, blue atoms are Ni and silver atoms are Pt. Adapted from Ref. [81].

## 4. HER on AuPd alloys: the ensemble effect and adsorbate-induced ensemble formation

### 4.1 Introduction to AuPd alloys

The adsorption and catalytic properties of Au/Pd systems have been investigated in the context of a variety of chemical reactions for more than two decades [82]. Because of the strong dependence of their catalytic activity on the atomic structure and composition of the catalytic surface, they have provided an ideal model system for investigating a wide range of (electro)catalytic reactions [83]. Indeed, a plethora of diverse structures have been fabricated [84], including heteroepitaxial layers ranging from submonolayers [85-86] to multilayers [82], decorated defects (e.g. steps [87]), adsorbed nanostructures [88-89], and alloyed nanoparticles [90]. This rich variety of alloy structures is met with an equally rich selection of (electro)chemical reactions which have been characterized on AuPd (electro)catalysts [82]. Among these, the hydrogen evolution reaction (HER) has attracted particular attention [82-83, 86, 91].

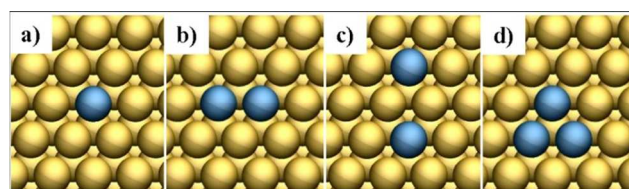


**Figure 12:** Examples of Pd ensembles in a Au(111) surface: **a)** monomer, **b)** dimer, **c)** monomer pair and **d)** trimer. Blue atoms are Pd and gold atoms are Au.

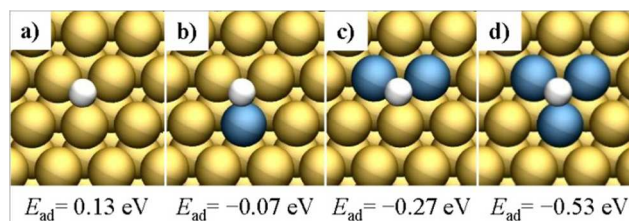


**Figure 13** Hydrogen adsorption on a Au(111) surface with various Pd ensembles: **a)** no Pd, **b)** Pd monomer, **c)** Pd dimer and **d)** Pd trimer. Adsorption energies are from DFT and referenced to gas phase  $\text{H}_2$ . Adapted from Ref. [93]. White atoms are H, blue atoms are Pd and gold atoms are Au.

### 4.2 Ensemble effect

One of the recurring themes in studies of AuPd surface alloys is the ensemble effect, in which specific geometric groupings of atoms at the surface function as adsorption or catalytic active sites [8, 91-93]. Temperature programmed desorption (TPD) studies of preadsorbed CO on AuPd alloyed surfaces provide an illustrative example of this effect. Because CO does not adsorb on a pure Au(111) surface, its adsorption on AuPd is attributed to the presence of Pd atoms. A single Pd atom (i.e. a Pd surface monomer) suffices to support CO adsorption; however, stronger adsorption takes place when coordination to two adjacent Pd atoms is made possible via a Pd surface dimer. Adsorption at a Pd trimer is even stronger. (See **Figure 12** for examples of these and other Pd surface ensembles). These three different types of adsorption sites are reflected in three different TPD peaks, which can be used to determine the populations of Pd monomers, dimers and trimers [94-95].

Ethylene dehydrogenation on AuPd is another example of a catalytic reaction governed by an ensemble effect. Here pairs of adjacent Pd atoms (i.e. Pd dimers) serve as the active site, enabling the C atoms to transform their C-C  $\pi$ -bond into a pair of  $\sigma$ -bonds, one with each of the Pd atoms in the dimer [94]. In a third example, an experimental study of the synthesis of vinyl acetate on AuPd alloys with various surface compositions suggested that a pair of noncontiguous Pd surface monomers is the critical ensemble for catalytically supporting this reaction [92]. As a final example, the reactivity of AuPd surface structure with hydrogen has been studied extensively [82-83, 91, 93, 96-97]. While Pd surface dimers are believed to be the critical (i.e. minimal in this case) ensemble for the underpotential deposition of hydrogen [8], monomers appear to furnish the active sites in the hydrogen evolution reaction [91]. **Figure 13** illustrates how DFT calculations have been used to evaluate the increase in hydrogen adsorption energy as the number of Pd atoms directly coordinated with the hydrogen adsorbate increases from zero to three [93].

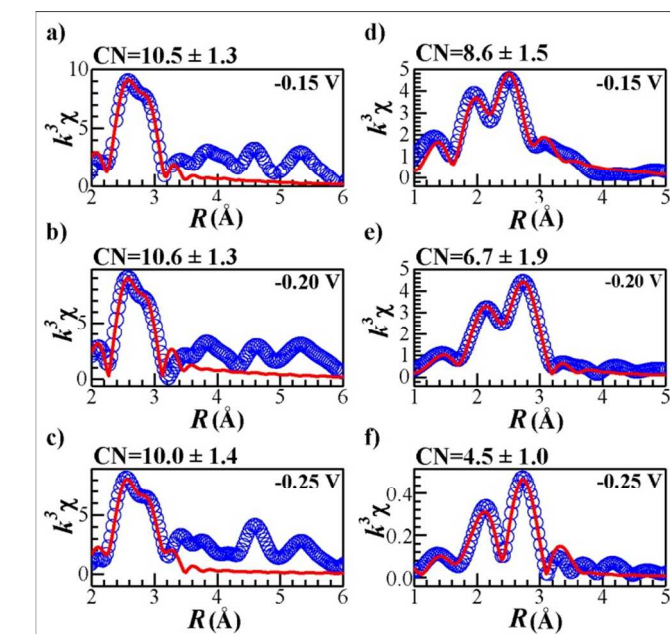


**Figure 14**  $k^3$ -normalized EXAFS functions extracted from X-ray absorption spectra collected at Au L3 for controlled potentials: **a)**  $-0.15$  V, **b)**  $-0.20$  V and **c)**  $-0.25$  V, and at the Pd K-edge for the same controlled potentials: **d)**  $-0.15$  V, **e)**  $-0.20$  V and **f)**  $-0.25$  V. Solid lines show the NLLS fits of the local structure refinement. The coordination numbers (CN) from the NLLS fits are given above the plot. Adapted from Ref. [97].

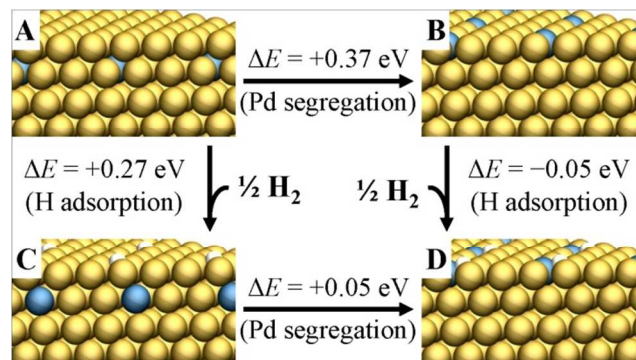


**Figure 15** Schematic with energies for hydrogen adsorption and Pd surface segregation involving a Pd monomer at or near the Au(111) surface. White atoms are H, blue atoms are Pd and gold atoms are Au.

### 4.3 Adsorbate-induced ensemble formation

To investigate the dynamic nature of AuPd systems *in-situ* EXAFS data were collected and analyzed in a manner similar to the data for the Pt<sub>3</sub>Ni system. Along these lines *in-situ* X-ray absorption spectroscopy was recently used to track surface segregation in Au<sub>4</sub>Pd nanoparticles during potential driven hydrogen adsorption [97]. Due to the overall chemical composition of the nanoparticles, their dynamic nature is reflected most clearly in the local environment of Pd, where the Pd EXAFS functions prove to be highly sensitive to hydrogen adsorption and thus reflect a change in the surface composition triggered by hydrogen adsorption (see **Figure 14**). In particular, when the applied electrode potential is set to values corresponding to hydrogen adsorption/evolution, the average coordination number of Pd decreases with decreasing electrode potential from ca. 8.6 ( $-0.15$  V vs. SCE) to ca. 4.5 ( $-0.25$  V vs. SCE). Furthermore the absorbing Pd atoms appear to be coordinated an average of one hydrogen (with the bonding distance of 1.82 Å) and have two types of metal neighbors, whose distances change from 2.77 Å and 2.98 Å (at  $-0.15$  V vs. SCE) to 2.81 and 3.46 Å (at  $-0.25$  V vs SCE). These local arrangements differ significantly from known palladium hydride phases (thus ruling out the formation of a palladium hydride phase) and reflect an extensive transfer of Pd to the surface, presumably to maximize the number of Pd-H interactions. The experimentally obtained *average* Pd coordination number of 4.5 is significantly lower than expected for atoms confined to low index surfaces (i.e. 8–9). Thus, the coordination numbers strongly suggests the complete confinement of the Pd atoms to the surface, forming a stable core-shell like arrangement, at intermediate potentials (near  $-0.15$  V vs. SCE), followed by the confinement of Pd to even lower coordination sites (e.g. steps or edges) and possible formation of Pd surface structures with ultra-low coordination numbers (e.g. adatoms) as the potential is further decreased ( $E < -0.25$  V vs. SCE).

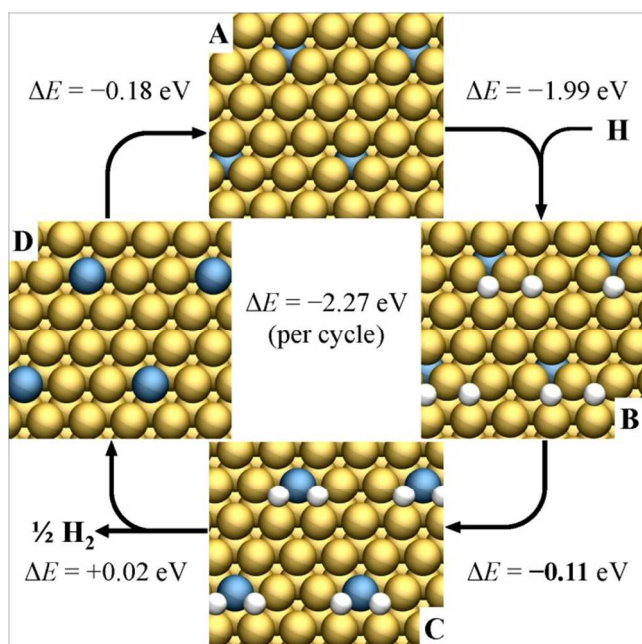


**Figure 16** Scheme of reversible surface monomer formation on a AuPd catalyst (111) during the hydrogen evolution reaction when the hydrogen coverage is double the number of Pd atoms at or near the surface. State A is the equilibrium state in the absence of adsorbates. State B is the metastable state immediately following hydrogen adsorption, but before the catalyst has rearranged itself. State C is the equilibrium state of the catalyst with adsorbed hydrogen. State D is the metastable state of the catalyst following the departure of  $\text{H}_2$  gas from the surface. The conversion of hydrogen atoms to  $\text{H}_2$  gas results in an energy gain of 2.27 eV per hydrogen atom (the energy gain per cycle). All energies (eV) are computed per hydrogen atom. White atoms are H, blue atoms are Pd and gold atoms are Au.

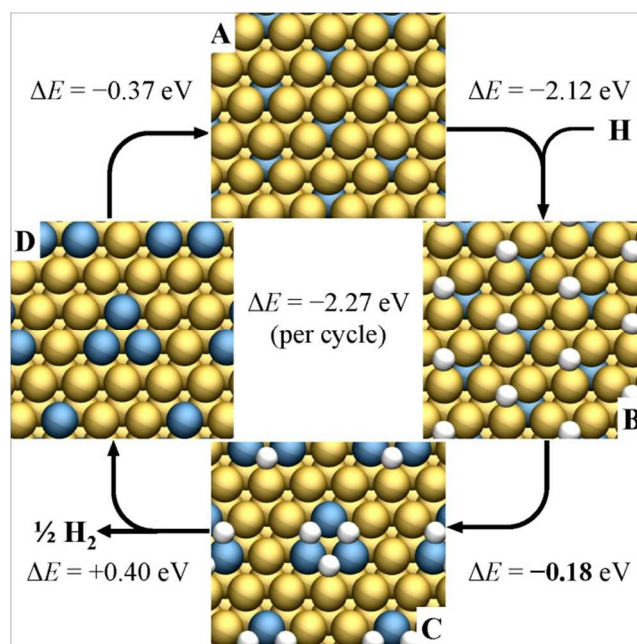


**Figure 17** Scheme of reversible surface trimer formation on AuPd catalyst (111) during the hydrogen evolution reaction when the hydrogen coverage is equal to the Pd concentration at or near the surface. State A is the equilibrium state in the absence of adsorbates. State B is the metastable state immediately following hydrogen adsorption, but before the catalyst has had a chance to rearrange itself. State C is the equilibrium state of the catalyst with adsorbed hydrogen. State D is the metastable state of the catalyst following the evolution of  $\text{H}_2$  gas from the surface. The conversion of hydrogen atoms to  $\text{H}_2$  gas results in an energy gain of 2.27 eV per hydrogen atom (the energy gain per cycle). All energies (eV) are computed per hydrogen atom. White atoms are H, blue atoms are Pd and gold atoms are Au. Adapted from Ref. [97].

In order to provide independent evidence for this interpretation of the experimental results and gain additional insight into the detailed atomistic mechanisms involved, a series of DFT calculations were performed to investigate hydrogen-adsorbate-induced surface segregation in AuPd alloys [97]. A Au(111) surface described using a ( $p3 \times 3$ ) unit cell was chosen as a first approximation of the nanoparticle surface, which is expected to involve other faces along with edges, corners and possibly other defects. In the absence of adsorbed hydrogen a Pd monomer is found to prefer occupying a subsurface site by  $\Delta E = 0.37$  eV over a surface site, as shown in **Figure 15**. The adsorption of one hydrogen atom per Pd monomer decreases the favorability of subsurface Pd to  $\Delta E = 0.06$  eV, but bringing the Pd monomer to the surface is still unfavorable. The adsorption of an additional hydrogen atom is able to reverse the trend so that a pair of hydrogen atoms stabilizes surface Pd by  $-0.11$  eV (see **Figure 16**).

Alternatively, three hydrogen atoms are able to cooperate and draw three Pd atoms to the surface to form a surface trimer with an energy gain of  $\Delta E = -0.18$  eV per hydrogen atom (see **Figure 17**). Thus, adsorbed hydrogen atoms are not only responsible for bringing Pd to the surface, but also for the formation of Pd trimers, which in the absence of the adsorbed hydrogen are  $\Delta E = 0.06$  eV less stable than three non-interacting Pd monomers. If the hydrogen leaves the surface, then the surface Pd (as either monomers or trimers) becomes thermodynamically unstable so that migration of Pd into the subsurface to form subsurface monomers is exothermic ( $\Delta E = -0.37$  eV and  $\Delta E = -0.18$  eV per previously involved hydrogen for the two cases respectively). Thus, on the assumption that segregation is not kinetically hindered (which would appear to be the case based on experimental observations of nanoparticles), then Pd moves between the surface and subsurface layers as hydrogen is adsorbed and desorbed/evolved.

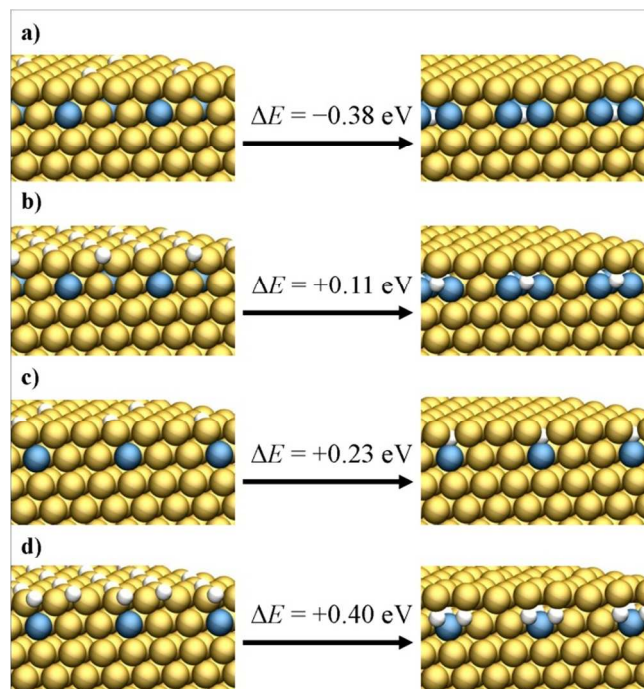


**Figure 18** Energies for the formation of subsurface palladium hydride from adsorbed hydrogen and subsurface Pd for various concentrations of Pd at or near the surface and various coverages of adsorbed hydrogen: a) 1:3 H:Pd ratio with 1/9 ML adsorbed hydrogen, b) 1:1 H:Pd ratio with 1/9 ML adsorbed hydrogen, c) 1:1 H:Pd ratio with 1/3 ML adsorbed hydrogen, d) 3:1 H:Pd ratio with 1/3 ML adsorbed hydrogen. All energies (eV) are computed per hydrogen atom. White atoms are H, blue atoms are Pd and gold atoms are Au.

However, there is another possibility which we ought to consider: namely, that the attraction between hydrogen and Pd could result in subsurface hydrogen, rather than surface Pd. As illustrated in **Figure 18**, this was only found to be the case for low hydrogen to Pd ratios. Thus, three Pd subsurface monomers are able to cooperate to draw a single hydrogen atom into a subsurface interstitial position between them. Interestingly, this means that the Pd atoms lose their status as monomers as they now form a subsurface trimer, which is then ready to be drawn to the surface by the appearance of additional hydrogen adsorbates.

Combining the EXAFS and DFT results we arrive at the following, most probable atomistic description of adsorbate-induced ensemble formation. The most stable surface of the Au<sub>4</sub>Pd particle is pure Au prior to the adsorption of hydrogen, with subsurface Pd atoms avoiding each others, and thus forming subsurface monomers. The adsorption of small quantities of hydrogen, leads to hydrogen absorption into the subsurface, where a stabilizing Pd trimer is gathered around each subsurface hydrogen atom. As the number of ad- and absorbed hydrogen atoms approaches the number of subsurface Pd atoms, these Pd subsurface trimers are drawn to the surface. However, the adsorption of additional hydrogen encourages the breakup of the trimers into monomers, because monomers enable a greater number of hydrogen atoms to bond with Pd (up to three hydrogen adsorbates per Pd monomer instead of just one or two). The migration of Pd to even lower-coordination sites (e.g. edges, steps, corners, adatoms) is needed to allow for more than three hydrogen atoms to coordinate with each Pd and is supported by the very low Pd-M coordination numbers obtained from the

analysis of the EXAFS data.

## 5. Concluding Remarks

### 5.1 Indispensability of rational design

Bimetallic alloys exhibit a spectrum of electrochemical and catalytic characteristics that go far beyond those of unalloyed metals. The numerous combinations and nearly endless array of conceivable compositions and structures (see Ref. [98] for an overview of surface morphologies of bimetallic alloys as well as the discussion of additional complicating factors) for each composition might tantalize one with the thought that for many an application a better bimetallic material (i.e. a new composition and/or structure) is out there, just waiting to be synthesized or discovered. Yet the same overabundance of variation that would seem to guarantee the existence of a better bimetallic surface for a given application turns the search for the optimal materials into a game of finding the needle in a haystack. Strategies for the rational design of electrode and catalyst materials are needed in order to quickly focus on promising candidate materials and improve their performance in an informed rather than haphazard manner.

The proper foundation for rational design is a fundamental understanding of the functionality of candidate materials. This entails a detailed understanding of the atomistic mechanisms for all relevant processes. The study of model systems is indispensable for laying this foundation, because it allows for the isolation and subsequent elucidation of the effects of individual structural and compositional parameters. In other words, model systems can help isolate the structures and behaviors of a material which are essential for its functionality. In discussing three particular model systems one of the central aims of this perspective has been to highlight behaviours that are essential to the functionality of bimetallic systems in general, and thus need to be considered in efforts to understand other systems as well. Therefore, insofar as these behaviors are critically involved in determining the functionality of bimetallic materials, the successful rational design of catalyst and electrode materials cannot proceed without taking them into account.

### 5.2 Considering structural stability

In light of the very real danger of catalyst degradation, the importance of structural stability has long been a central concern, particularly in the fuel cell community. In this context, it is not just the macroscopic material, but the catalytically active surface structure itself, which must be stable under catalytic conditions. Adsorbed intermediates are an intrinsic part of heterogeneous (electro)catalysis, and so the possibility of adsorbate-induced surface segregation or ensemble formation is unavoidable. A first implication of this possibility is that mechanistic models and studies must identify the surface structure relevant to catalytic conditions and then investigate the reaction on this surface, since it is the only available surface for catalysis. A second implication is that surface stability in the presence of adsorbed intermediates (i.e. under the conditions under which catalysis takes place) must be taken into account during rational catalyst design, because only surface structures that are realizable under reaction conditions are viable candidates. On one hand, this might mean that the “ideal” surface structure is unstable and thus unrealizable

under reaction conditions. On the other hand, the “ideal” surface might be formed *in operando* so that only the proper precursor system needs synthesized or prepared beforehand.

### 5.3 Synthesizing surface structures

The close relationship between the atomic structure and functional performance of a surface stresses the fact that successful surface synthesis is an indispensable aspect of the development of improved electrodes and catalysts. One would expect that obtaining such a high degree of synthetic control (e.g. to produce surface ensembles) would be likely to pose a significant challenges. While there will certainly be challenges along these lines, there are two considerations which could work to one’s benefit in the task of synthesizing newly designed surface structures. First, if rational design limits itself to surface structures, which are stable under operating conditions, then fruitless attempts to synthesize unstable surfaces will be avoided. Second, it may not be necessary to directly synthesize the desired surface. Instead, the synthesis of a precursor, which automatically transforms *in operando* into the desired surface, may suffice.

### 5.4 Delving into the dynamics

An important theme that has already been touched on several times is the dynamic, as opposed to static, nature of the bimetallic surface. Indeed the presence of adsorbed intermediates or other adsorbates is capable of exerting a profound influence on the surface structure of a bimetallic alloy. Possible results include a change in the atomic composition at the surface (i.e. adsorbate-induced surface segregation), the formation of a particular ensemble (i.e. adsorbate-induced ensemble formation), a change in the relative stabilities of the different surfaces faces, and the stabilization of defects or new surface structures (e.g. steps, adatoms or surface buckling). Thermodynamic favorability requires that a decrease in the surface free energy upon the adsorption of intermediates drive transformation of the surface into its active structure, while a similar decrease in free energy drives the vacated surface to revert to its original structure. Kinetic feasibility requires that the reaction energy barriers for these surface transformations are low enough for them to take place within the timeframe of the surface’s exposure to the reactive environment. Obviously, a metastable structure could be either advantageous (e.g. if it is more catalytically active than the kinetically hindered global structure) or disadvantageous if the structure corresponding to the global minimum is desired. In either case, a full understanding of the functionality of a bimetallic surface subject to some form of adsorbate-induced surface segregation requires not only a knowledge of the thermodynamics of catalyst dynamics, but also an understanding of the kinetics relevant to these changes. Delving into this kinetic aspect of surface dynamics is one of the most exciting challenges facing researchers seeking to unlock the secrets of bimetallic electrodes and catalysts, and is likely to play an important role in the further development of nanostructured electrodes and catalysts for all sorts of diverse applications.

### Acknowledgements

We gratefully acknowledge financial support from the Deutsche Forschungsgemeinschaft (DFG) through FOR-1376 (Elementary

reaction steps in Electrochemistry: Theory meets Experiment). JEM gratefully acknowledges the Alexander von Humboldt Foundation for financial support. PK gratefully acknowledges the support of the Deutsches Elektronen Synchrontronen (project 11734) and of Brookhaven National Laboratory (project 17851). Support from the European Union through the ERC-Starting Grant THEOFUN (Grant-Agreement No. 259608) is also gratefully acknowledged.

### Notes and references

- <sup>65</sup> Institut für Elektrochemie, Universität Ulm, Albert-Einstein-Allee 47, 89081 Ulm, Germany. Fax: 49 7315 025409; Tel: 49 7315 025401; E-mail: [timo.jacob@uni-ulm.de](mailto:timo.jacob@uni-ulm.de)
- <sup>b</sup> J. Heyrovský Institute of Physical Chemistry, Dolejškova 3, Prague 18223, Czech Republic.
- H. Gerischer, *Bull. Soc. Chim. Belg.*, 1958, **67**, 506.
- R. Parsons, *Trans. Faraday Soc.*, 1958, **54**, 1053.
- S. Trasatti, *J. Electroanal. Chem.*, 1972, **39**, 163.
- J.K. Nørskov, T. Bligard, A. Logardottir, J. R. Kitchin, J. G. Chen, S. Pandalov, and U. Stimming, *J. Electrochem. Soc.*, 2005, **152**, J. 23.
- W. Schmickler, S. Trasatti, *J. Electrochem. Soc.*, 2006, **153**, L31.
- R. Parsons, “Volcano Curves in Electrochemistry,” in: *Catalysis in Electrochemistry* (Eds. E. Santos, W. Schmickler), Wiley-VCH, 2011, p. 1-16.
- Jackson, V. Viswanathan, A.J. Forman, A.H. Larsen, J.K. Nørskov, T.F. Jaramillo, *ChemElectroChem*, 2014, **1**, 67–71.
- F. Maroun, F. Ozanom, O.M. Magnussen, R.J. Behm, *Science*, 2001, **293**, 1811-1814
- Watanabe, S. Motoo, *J. Electroanal. Chem.*, 1975, **60**, 259–266.
- M. Watanabe, S. Motoo, *J. Electroanal. Chem.*, 1975, **60**, 267–274.
- M. Watanabe, S. Motoo, *J. Electroanal. Chem.*, 1975, **60**, 275–283.
- H.A. Gasteiger, N. Markovic, P.N. Ross, E.J. Cairns, *J. Phys. Chem.*, 1993, **97**, 12020–12029.
- H.A. Gasteiger, N. Markovic, P.N. Ross, E.J. Cairns, *J. Phys. Chem.*, 1994, **98**, 617–625.
- H.A. Gasteiger, N. Markovic, P.N. Ross, E.J. Cairns, *Electrochim. Acta.*, 1994, **39**, 1825–1832.
- N.M. Markovic, H. A. Gasteiger, P. N. Ross, X. Jiang, I. Villegas, M. J. Weaver, *Electrochim. Acta*, 1995, **40**, 91–98.
- Hammer, J.K. Nørskov, *Surf. Sci.*, 1995, **343**, 211–220.
- J. Greeley, J.K. Nørskov, M. Mavrikakis *Annu. Rev. Phys. Chem.*, 2002, **53**, 319–348.
- V.R. Stamenkovic, B.S. Mun, K.J.J. Mayrhofer, P.N. Ross, N.M. Marković, J. Rossmeisl, J. Greeley, J.K. Nørskov, *Angew. Chem. Int. Ed.*, 2006, **45**, 2897–2901.
- G. Kyriakou, M.B. Boucher, A.D. Jewell, E.A. Lewis, T.J. Lawton, A.E. Baber, H.L. Tierney, M. Flytzani-Stephanopoulos, E.C.H. Sykes, *Science*, 2012, **335**, 1209–1212.
- J.M. Thomas, *PhysChemChemPhys*, 2014, **16**, 7647–7661.
- F. Tao, M.E. Grass, Y. Zhang, D.R. Butcher, J.R. Renzas, Z. Liu, J.Y. Chung, B.S. Mun, M. Salmeron, G.A. Somorjai, *Science*, 2008, **322**, 932–934.
- C. Cui, M. Ahmadi, R. Behafarid, L. Gan, M. Neumann, M. Heggen, B.R. Cuenya, P. Strasser, *Faraday Discuss.*, 2013, **162**, 91–112.
- J.A. Rodriguez, *Surf. Sci. Reports*, 1996, **24**, 223–287
- M.A. Vasiliev, *J. Phys. D: Appl. Phys.*, 1997, **30**, 3037–3070.
- R. Ferrando, J. Jellinek, R.L. Johnston, *Chem. Rev.*, 2008, **108**, 845–910
- H.-L. Jiang, Q. Xu, *J. Mater. Chem.*, 2011, **21**, 13705–13725.
- Wang, Y. Li, *Adv. Mater.*, 2011, **23**, 1044–1060
- J. Bockris, H. Wroblowa, *J. Electroanal. Chem.*, 1964, **7**, 428–451.
- O.A. Petry, B.I. Podlovchenko, A.N. Frumkin, H. Lal, *J. Electroanal. Chem.* **1965**, **10**, 253–269.
- B.R. Rauhe, F.R. McLarnon, E.J. Cairns, *J. Electrochem. Soc.*, 1995, **142**, 1073–1084.
- T.J. Schmidt, M. Noeske, H. A. Gasteiger, R. J. Behm, P. Britz, H. Bönemann, *J. Electrochem. Soc.*, 1998, **145**, 925–931.

- 32 N.M. Markovic, T. J. Schmidt, B. N. Grgur, H. A. Gasteiger, R. J. Behm, P. N. Ross, *J. Phys. Chem. B*, 1999, **103**, 8568–8577.
- 33 A. Hamnett in *Interfacial Electrochemistry: Theory, Experiment, and Applications* (Ed.: A. Wieckowski), Marcel Dekker, New York, 1999, 843–883.
- 5 34 S. R. Brankovic, N. S. Marinkovic, J. X. Wang, R. R. Adzic, *J. Electroanal. Chem.*, 2002, **532**, 57–66.
- 35 P. Waszczuk, G. Q. Lu, A. Wieckowski, C. Lu, C. Rice, R. I. Masel, *Electrochim. Acta*, 2002, **47**, 3637–3652.
- 10 36 K.A. Friedrich, K.P. Geyzers, U. Linke, U. Stimming, J. Stumper, *J. Electroanal. Chem.*, 1996, **402**, 2, 123–128.
- 37 W. F. Lin, M. S. Zei, M. Eiswirth, G. Ertl, T. Iwasita, W. Vielstich, *J. Phys. Chem. B*, 1999, **103**, 6968–6977.
- 38 K.A. Friedrich, K.P. Geyzers, A. Marmann, U. Stimming, R. Vogel, *Z. Phys. Chem.*, 1999, **208**, 137–150.
- 15 39 H. Massong, H. S. Wang, G. Samjeske, H. Baltruschat, *Electrochim. Acta*, 2000, **46**, 701–707.
- 40 T. Iwasita, H. Hoster, A. John-Anacker, W. F. Lin, W. Vielstich, *Langmuir*, 2000, **16**, 522–529.
- 20 41 H. Hoster, T. Iwasita, H. Baumgärtner, W. Vielstich, *Phys. Chem. Chem. Phys.*, 2001, **3**, 337–346.
- 42 Y. Tong, H. S. Kim, P.K. Babu, P. Waszczuk, A. Wieckowski, E. Oldfield, *J. Am. Chem. Soc.*, 2002, **124**, 468–473.
- 43 G.-Q. Lu, P. Waszczuk, A. Wieckowski, *J. Electroanal. Chem.*, 2002, **532**, 49–55.
- 25 44 N. P. Lebedeva, M. T. M. Koper, J. M. Feliu, R. A. van Santen, *J. Electroanal. Chem.*, 2002, **524–525**, 242–251.
- 45 C. Roth, N. Benker, T. Buhmester, M. Mazurek, M. Loster, H. Fuess, D.C. Koningsberger, D.E. Ramaker, *J. Am. Chem. Soc.*, 2005, **127**, 14607–14615.
- 30 46 L.A. Kibler, A.M. El-Aziz, R. Hoyer, D. M. Kolb, *Angew. Chem.*, 2005, **117**, 2116–2120; *Angew. Chem. Int. Ed.*, 2005, **44**, 2080–2084.
- 47 J.L. Zhang, M.B. Vukmirovic, Y. Xu, M. Mavrikakis, R.R. Adzic, *Angew. Chem.*, 2005, **117**, 2170–2173; *Angew. Chem. Int. Ed.*, 2005, **44**, 2132–2135.
- 35 48 T. Diemant, T. Hager, H. E. Hoster, H. Rauscher, R. J. Behm, *Surf. Sci.*, 2003, **541**, 137–146.
- 49 B.D. McNicol, R. T. Short, *J. Electroanal. Chem.*, 1977, **81**, 249–260.
- 40 50 H.A. Gasteiger, P.N. Ross, E.J. Cairns, *Surf. Sci.*, 1993, **293**, 67–80.
- 51 A.M. El-Aziz, R. Hoyer, L. A. Kibler, *ChemPhysChem*, 2010, **11**, 2906–2911.
- 52 Groß, *Topics Catal.*, 2006, **37**, 29–39.
- 53 Schlapka, M. Lischka, A. Groß, U. Käsberger, P. Jakob, *Phys Rev B*, 2003, **91**, 016101.
- 45 54 H.E. Hoster, O.B. Alves, M.T.M. Koper, *ChemPhysChem*, 2010, **11**, 1518–1524.
- 55 E.A. Heider, Diploma Thesis, 2011, University of Ulm.
- 56 Santos, P. Quaino, W. Schmickler, *Electrochimica Acta*, 2010, **55**, 4346–4352.
- 50 57 T.A. Maark, A.A. Peterson, *J. Phys. Chem. C*, 2004, **118**, 4275–4281.
- 58 J.A. Keith, T. Jacob, *Angew. Chem. Int. Ed.*, 2010, **49**, 9521–9525.
- 59 J.A. Keith, G. Jerkiewicz, T. Jacob, *ChemPhysChem*, 2010, **11**, 2779–2794.
- 55 60 S. Brimaud, A.K. Engstfeld, O.B. Alves, H.E. Hoster, R.J. Behm *Topics Catal.*, 2014, **57**, 222–235.
- 61 A. Appleby, F. Foulkes, *Fuel Cell Handbook*, Van Nostrand Reinhold: New York, 1989.
- 62 K. Kordesch, G. Simader, *Fuel Cells and Their Applications*, VCH: New York, 1996.
- 60 63 V.R. Stamenković, T. J. Schmidt, P. N. Ross, N. M. Marković, *J. Phys. Chem. B*, 2002, **106**, 11970–11979.
- 64 V.R. Stamenković, B. Fowler, B.S. Mun, G. F. Wang, P.N. Ross, C.A. Lucas, N.M. Marković, *Science*, 2007, **315**, 493–497.
- 65 65 N. P. Brandon, S. Skinner, B.C.H. Steele, *Annu. Rev. Mater. Res.*, 2003, **33**, 183–213.
- 66 V. Mehta, J.S.J. Cooper, *Power Sources*, 2003, **114**, 32–53.
- 67 J. Greeley, I. E. L. Stephens, A. S. Bondarenko, T. Johansson, H. A. Hansen, T. F. Jaramillo, J. Rossmeisl, I. Chorkendorff, J. K.Nørskov, *Nature Chem.*, 2009, **1**, 552–556.
- 68 J.K. Nørskov, T. Bligaard, J. Rossmeisl, C. H. Christensen, *Nat. Chem.*, 2009, **1**, 37–46.
- 69 T. Wadayama, N. Todoroki, Y. Yamada, T. Sugawara, K. Miyamoto, Y. Iijama, *Electrochem. Comm.*, 2010, **12**, 1112.
- 75 70 Y. Sha, T.H. Yu, B.V. Merinov, P. Shirvanian, W.A. Goddard, *J. Phys. Chem. C*, 2012, **116**, 21334.
- 71 J. Greeley, J.K. Nørskov, *J. Phys. Chem. C*, 2009, **113**, 4932–4939.
- 72 H. Yang, W. Vogel, C. Lamy, N. Alonso-Vante, *J. Phys. Chem. B* 2004, **108**, 11024–11034.
- 80 73 T. Jacob, W.A. Goddard III, *J. Phys. Chem. B*, 2004, **108**, 8311–8323.
- 74 T. Jacob, B.V. Merinov, W.A. Goddard III, *Chem. Phys. Lett.*, 2004, **385**, 374–377.
- 75 Y. Gauthier, Y. Joly, R. Baudoing, J. Rundgren, *Phys. Rev. B*, 1985, **31**, 6216–6218.
- 85 76 Y. Gauthier, *Surf. Rev. Lett.*, 1996, **3**, 1663–1689.
- 77 U. Bardi, A. Atrei, E. Zanazzi, G. Rovida, P. N. Ross, *Vacuum* 1990, **41**, 437–440.
- 78 U. Bardi, B. C. Beard, P. N. Ross, *J. Catal.*, 1990, **124**, 22–29.
- 90 79 S. Deckers, F.H.P.M. Habraken, W.F. Vanderweg, A.W.D. Vandergon, B. Pluis, J.F. Vanderveen, R. Baudoing, *Phys. Rev. B*, 1990, **42**, 3253–3259.
- 80 T.H. Yu, Y. Sha, B.V. Merinov, W.A. Goddard, *J. Phys. Chem. C*, 2010, **114**, 11527–11533.
- 95 81 H. Hoffmannová, M. Okube, V. Petrykin, P. Krtil, J.E. Mueller, T. Jacob *Langmuir*, 2013, **29**, 9046–9050.
- 82 L.A. Kibler, *Electrochim. Acta*, 2008, **53**, 6824–6828.
- 83 M.E. Björketun, G.S. Karlberg, J. Rossmeisl, I. Chorkendorff, H. Wolfschidt, U. Stimming, J.K. Nørskov, *Phys. Rev. B*, 2011, **84**, 045407.
- 100 84 P.J. Schäfer, L.A. Kibler, *Phys. Chem. Chem. Phys.*, 2010, **12**, 15225–15230.
- 85 J. Tang, M. Petri, L.A. Kibler, D.M. Kolb, *Electrochim. Acta*, 2005, **51**, 125–132.
- 105 86 L.A. Kibler, *ChemPhysChem*, 2006, **7**, 985–991.
- 87 J. Steidtner, F. Hernandez, H. Baltruschat, *J. Phys. Chem. C*, 2007, **111**, 12320–12327.
- 88 J. Tang, M. Petri, L.A. Kibler, D.M. Kolb, *Acta Phys. Chim. Sin.*, 2005, **21**, 1303–1306.
- 110 89 D.M. Kolb, F.C. Simeone, *Electrochim. Acta*, 2005, **50**, 2989–2996.
- 90 D. Wang, A. Villa, F. Porta, D. Sua, L. Prati, *Chem. Commun.*, 2006, **18**, 1956.
- 91 Y. Pluntke, L.A. Kibler, D.M. Kolb, *Phys. Chem. Chem. Phys.*, 2008, **10**, 3684–3688.
- 115 92 M. Chen, D. Kumar, C.-W. Yi, D. W. Goodman, *Science*, 2005, **310**, 291–293.
- 93 S. Venkatachalam, T. Jacob, *Phys. Chem. Chem. Phys.*, 2009, **11**, 3263–3270.
- 94 K. Luo, T. Wei, C.-W. Yi, S. Axnanda, D.W. Goodman, *J. Phys. Chem. B*, 2005, **109**, 23517–23522.
- 120 95 M. Ruff, N. Takehiro, P. Liu, J.K. Nørskov, R.J. Behm, *ChemPhysChem*, 2007, **8**, 2068–2071.
- 96 P. Quaino, E. Santos, H. Wolfschmidt, M.A. Montero, U. Stimming, *Catal. Today*, 2011, **177**, 55–63.
- 125 97 M. Okube, V. Petrykin, J.E. Mueller, D. Fantauzzi, P. Krtil, T. Jacob, *ChemElectroChem*, 2014, **1**, 207–212.
- 98 F. Calle-Vallejo, M.T.M. Koper, A.S. Bandarenka, *Chem. Soc. Rev.*, 2013, **42**, 5210–5230.